CHEMISTRY OF MATERIALS
Cite This: *Chem. Mater.* 2018, 30, 8897−8904
Article
pubs.acs.org/cm

Synthesis of Fine-Tuning Highly Magnetic Fe@Fe_xO_y Nanoparticles through Continuous Injection and a Study of Magnetic Hyperthermia

Simone Famiani,[†,‡] Alec P. LaGrow,[†,‡] Maximilian O. Besenhard,[§] Shinya Maenosono,*[,∥] and Nguyen Thi Kim Thanh*[,†,‡]

[†]Biophysics Group, Department of Physics and Astronomy, University College London (UCL), Gower Street, London WC1E 6BT, U.K.

[‡]Healthcare Biomagnetic and Nanomaterials Laboratories, University College London (UCL), 21 Albemarle Street, London W1S 4BS, U.K.

[§]Department of Chemical Engineering, University College London (UCL), Torrington Place, London WC1E 7JE, U.K.

[∥]School of Materials Science, Japan Advanced Institute of Science and Technology (JAIST), 1-1 Asahidai, Nomi, Ishikawa 923-1292, Japan

Supporting Information

ABSTRACT: Core@shell Fe@Fe_xO_y nanoparticles (NPs) have the potential to be promising tools for many applications, thanks to their combination of an iron core, with a high magnetic moment and an iron oxide shell which could protect the core from oxidation. However, the deterioration of NPs structure can lead to the shrinking of the core and the hollowing of the structure, diminishing the magnetic properties. The ability to retain the iron core under biomedically compatible conditions is desirable for many applications. In this paper, we have developed a synthetic method to produce core@shell α-Fe@Fe_xO_y NPs with tunable sizes and evaluated the retention of the stable magnetic α-Fe core upon exposure to air and after ligand exchange and its resulting effect on the magnetic hyperthermia. In particular, using a continuous injection of the precursor, we were able to finely tune the final size of the core@shell NPs producing four samples with average sizes of 12, 15, 18, and 20 nm. The structural properties of the particles were studied, and while the size increases, the chemical stability of the iron core is enhanced, and the magnetic properties improved accordingly. Particles larger than 20 nm were shown to be prone to aggregation, resulting in an abrupt increase of the particle size distribution. Two samples with high magnetization saturation value and low polydispersity, 15 and 18 nm, were transferred in water using a dopamine-functionalized poly(isobutylene-*alt*-maleic anhydride) polymer, resulting in colloidal stability over a wide range of pH and ionic strength comparable to physiological conditions. We found that the 18 nm particles retain their chemical properties over 2 months, with less oxidation of the Fe core; this results in a specific absorption rate (SAR) value of 660 W g^{-1} and intrinsic loss power (ILP) of 3.6 nHm^2 kg^{-1}, while the 15 nm NPs resulted in the reduction of their properties due to oxidation of the core.

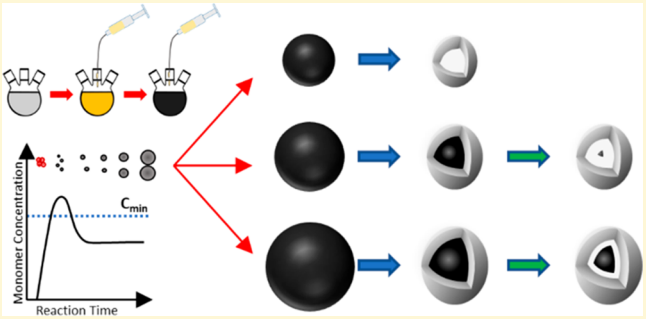

INTRODUCTION

Iron (Fe) nanoparticles (NPs) have been gathering much attention in the past few decades due to their intrinsically high saturation magnetization (M_s).[1] This is desirable for many biomedical applications such as magnetic hyperthermia, magnetic resonance imaging (MRI), magnetic cell separation, and targeted drug delivery.[2−9] In the case of magnetic hyperthermia the higher magnetic moment can result in better performances compared to relative oxides (magnetite or maghemite), and proof-of-concept demonstrations with Fe NPs have shown promising results.[10]

High-quality Fe NPs are typically synthesized in organic solvents where it is easier to control the crystal phase and size.[11] Once formed in solution, the metallic Fe NPs are partially oxidized to form an oxide layer on the surface by adding oxidizing agent[12] or simply exposing the solution to air.[13] This can act as a protective shell for the Fe core to suppress further oxidation. Before being used in biological conditions, Fe NPs need to be transferred into water, usually via ligand exchange of the surfactants bound to the iron oxide shell surface.[13] The effect of the latter process upon the chemical stability of the core@shell structure has been rarely

Received: September 25, 2018
Revised: November 19, 2018
Published: November 20, 2018

DOI: 10.1021/acs.chemmater.8b04056
Chem. Mater. 2018, 30, 8897−8904

taken into account, but this could potentially explain the divergence between hyperthermia outputs reported under vacuum conditions[7] and using nonoxidized Fe NPs vs the one reported after Fe NPs were transferred in water.[3]

Nemati et al. analyzed different sizes of Fe@Fe_3O_4 NPs between 8 and 14 nm for magnetic hyperthermia applications after being ligand exchanged.[14] The authors showed that for the larger core@shell NPs a better magnetic response and heating rate can be achieved after the transfer in water. This is due to a hollowing process known as the Kirkendall effect which they observed was size dependent and for smaller NPs (8 nm) results in completely hollow NPs in a few weeks. For larger NPs (≥14 nm) the process leaves parts of the core intact, but the residual Fe core exhibits only poor heating characteristic for magnetic hyperthermia applications. Therefore, larger Fe@Fe_3O_4 NPs are desirable for biomedical applications, allowing the oxidation of the shell without sacrificing significant fractions of the Fe core.

As previous studies showed, good size tunability with a narrow size distribution can be obtained through a continuous injection of precursor.[15] This can prevent the process of Ostwald ripening (or size defocusing) from taking place when the monomer is depleting. As more precursor is added in a later stage of the reaction, a process of refocusing of the NP size can be promoted.[16,17] In addition, one of the most recognized theories to describe the growth evolution of a colloidal system was proposed by LaMer,[18] suggesting that the excessive addition of precursor at a later stage (i.e., after initial particle formation) can lead to a second nucleation process if the concentration of monomer raises above the nucleation threshold (C_{min}). This is undesirable as the growth of two populations would lead to a broadening of the size distribution. By controlling the rate of addition, it is possible to prevent a second nucleation stage and promote just the growth of the crystals.

Herein, we report a simple yet effective way of controlling the size of crystalline α-Fe NPs for biomedical applications by using a sequential addition of iron precursor into the reaction solution. The value of M_s increases with the NP size, and the larger NPs are shown to retain their properties after ligand exchange, which makes them very useful for biomedical applications.

MATERIALS AND METHODS

Materials. 1-Octadecene (ODE, purity 90%), hexadecylamine (HDA, purity 90%), diethyl ether (anhydrous, purity ≥99.7%), hydrochloric acid (HCl, assay 37%), oleylamine (OAm, purity 70%), poly(isobutylene-*alt*-maleic anhydride) (PIMA, $M_w \approx 6000$), dopamine hydrochloride (DOPA), dimethylformamide (DMF, anhydrous), triethylamine, tetrahydrofuran (THF), and disodium tetraborate buffer solution were purchased from Sigma-Aldrich, Japan. Ethanol (EtOH, purity 99.5%) was obtained from Nacalai Tesque, Japan. Iron pentacarbonyl [$Fe(CO)_5$, purity >95%], hexane, and chloroform were obtained from Kanto Chemicals, Japan. All the reagents were used as purchased without any further purification.

Synthesis of Fe NPs. The Fe NPs were prepared by using OAm as a ligand and hexadecylamonium chloride (HDA-Cl) as an essential additive to control the decomposition rate of $Fe(CO)_5$ to obtain highly crystalline Fe NPs.[3] HDA-Cl was synthesized following a previously published procedure.[19] Typically, OAm (0.160 mL, 0.5 mmol), HDA-Cl (0.138 g, 0.5 mmol), and ODE (10 mL) were mixed in a 50 mL three-neck flask and degassed for 60 min at 120 °C under an Ar flux and vigorous magnetic stirring. After increasing the solution temperature to 180 °C, $Fe(CO)_5$ was added to the flask using a syringe pump (KD Scientific Inc., KDS100) at a rate of addition of 0.4 mL/h. The start of the reaction, t_0, was considered when the first drop of precursor was introduced into the reaction solution. The rate of addition of $Fe(CO)_5$ and the concentration of both OAm and HDA-Cl were kept constant in all the reactions, and different sizes of NPs were obtained by adding different amounts of iron precursor, i.e., extending the injection time. After addition of $Fe(CO)_5$, the solution typically turned black after about 15 min of injection, indicating the formation of Fe NPs. The longest reaction was run for 45 min, after which the injection and the heating were stopped, and the solution was allowed to cool at room temperature. Three other injections times were selected to obtain different sizes of NPs. The reaction conditions are summarized in Table 1 with the equivalent time of injection for each amount used. Afterward, the NPs were washed with a mixture of chloroform/ethanol (1:3 vol/vol) and centrifuged at 5000 rpm (4640 *g*) for 3 min. The supernatant was then discarded, and the process was repeated two times. The final precipitate was redispersed in chloroform.

Table 1. Amount of Iron Precursor and Relative Injection Time Used in the Four Reactions with the Corresponding NPs Size Obtained

amount of $Fe(CO)_5$ injected (mmol)	injection time (min)	final particle size (nm)
1.0	20	12.6
1.3	25	15.9
2.0	38	18.3
2.4	45	20.7

Characterization of Fe NPs. The crystalline structures of the resulting NPs were studied by a X-ray diffractometer (XRD, Rigaku MiniFlex600) using a Cu Kα source (λ = 1.5418 Å). The mean crystalline size was estimated from the obtained XRD pattern using the Scherrer formula (eq S1). The mean size, size distribution, and morphology of the NPs were examined with a transmission electron microscope (TEM, Hitachi H-7650) operated at an acceleration voltage of 100 kV. TEM samples were prepared by dropping the suspension of NPs onto a carbon-coated TEM grid and dried in air. A scanning TEM (STEM) equipped with a high-angle annular dark-field (HAADF) detector and energy-dispersive X-ray spectroscopy (EDS) was also used to further analyze the nanoscale structure of the NPs. HAADF-STEM imaging and EDS elemental mapping were performed on a JEOL JEM-ARM200F microscope operated at 200 kV with a spherical aberration corrector and a nominal resolution of 0.8 Å.

The magnetic properties of the NPs were evaluated with a hybrid superconducting quantum interference device−vibrating sample magnetometer (SQUID-VSM, Quantum Design). The compositions of the NPs were further analyzed using X-ray photoelectron spectroscopy (XPS) on a high-performance XPS system (Shimadzu Kratos, Axis-Ultra DLD) using Al Kα radiation.

The colloidal stability of the Fe NPs in an aqueous medium over a range of pH was investigated by monitoring the hydrodynamic size and zeta potentials of the NPs using the dynamic light scattering (DLS) technique with a Zetasizer Nano (Malvern Panalytical, UK). The effect of ionic strength in the medium on the stability of the NPs was also assessed by using NaCl at various concentrations.

The heating characteristics of the synthesized NPs were measured during exposure to ac magnetic fields of various frequencies and field strengths using a G2 driver D5 series calorimetric analyzer (nBnanoScale Biomagnetics, Spain). This analyzer used an optical fiber temperature probe immersed inside the Fe NPs, monitoring temperature variations during field exposure. The specific absorption rate [SAR (W g^{-1})] values were calculated as

$$\mathrm{SAR} = \frac{C}{m}\frac{\mathrm{d}T}{\mathrm{d}t}$$

where C is the specific heat capacity of water (4185 J L^{-1} K^{-1}) and m is the concentration (g L^{-1}) expressed in Fe present in the dispersion. The SAR value was then normalized with the field strength and

DOI: 10.1021/acs.chemmater.8b04056
Chem. Mater. 2018, 30, 8897−8904

frequency used in the measurement to obtain the intrinsic loss power [ILP ($nHm^2\ kg^{-1}$)].[20] This allows the direct comparison of results.

Ligand Exchange. The ligand exchange was performed by following a modified procedure previously reported and adapted to the current system.[21] Briefly, to obtain a dopamine-functionalized polymer with a limited number of anchor points, the synthesis was performed as follows: 0.770 g of PIMA (5 mmol monomer units) was dissolved in 10 mL of DMF in a 50 mL three-necked round-bottomed flask. After purging the solution with nitrogen, the temperature was raised to 70 °C. Then, 0.5 mL of DMF containing 0.25 mmol of DOPA, previously activated with triethylamine hydrochloride followed by centrifugation to remove the formed salts (e.g., triethylamine hydrochloride), was slowly injected into the solution using the syringe pump and left to react overnight. To collect the polymer, the DMF was first removed under vacuum and deionized water was used to precipitate the waxy product. The polymer was further washed using a 1 M HCl solution (three times) and deionized water and finally dried under vacuum.

The ligand exchange was performed as follows: First, 50 mg of polymer was added to 10 mL of THF containing a few drops of EtOH. The suspension was sonicated for 5 min until a clear solution was obtained. Second, about 10 mg of NPs was precipitated from the original dispersion in chloroform using EtOH and then dispersed in a few milliliters of THF. Subsequently, this nanoparticle dispersion was added to the polymer solution and left in a rotating shaker for 48 h. The sample was then precipitated using an excess of hexane and centrifuge for 2 min at 4000 rpm (2969 *g*). After the supernatant was discarded, 6 mL of THF and 1 mL of EtOH were added to redisperse the precipitate; excess of hexane was further used, and the turbid dispersion was centrifuged again. The supernatant was then discarded, and the precipitate was dried under vacuum, leaving a black pellet. This was finally transferred in 10 mL of disodium tetraborate buffer solution at pH = 9.2 and allowed to stir for 24−48 h in a rotating shaker after few minutes of sonication to help to break down the pellet into smaller pieces. Once the dispersion gets clear, indicating that water transfer was complete, a 0.45 μm disposable syringe filter with VWR poly(ether sulfone) membrane was used to remove any big aggregates, and the excess of ligands was removed through a centrifugal filter (Sartorius, M_w cutoff 50 kDa) by applying three to four rounds of concentration/dilution with Milli-Q water (>18.0 MΩ cm^{-1}).

RESULTS AND DISCUSSION

Synthesis of Fe NPs. To achieve control over the final size of Fe NPs, we used a continuous addition of $Fe(CO)_5$ precursor instead of a single injection. In Figure 1a, the schematic illustration of the setup is shown. In this approach the growth of the NPs is described through the extended LaMer plot configuration[15] (Figure 1b), where after the formation of the nuclei the growth continues through the addition of more Fe precursor. For the conditions reported here, the TEM images of the four samples show how the size of NPs increases with increasing the amount of Fe precursor added in the reaction solution (Figure 1c−f). The NPs synthesized using 1.0 mmol of $Fe(CO)_5$, which corresponds to 20 min injection time, have a mean diameter of 12.6 ± 0.6 nm as shown in Figure 1c. No core was observed, and the NPs appear to be fully oxidized after being exposed to air. When 1.3 mmol of $Fe(CO)_5$ was used (25 min of injection time), the NPs size increases to 15.9 ± 0.9 nm and the NPs deposit onto the grid forming a superlattice (Figure 1d,e), indicating a high uniformity in size. In this case, a distinct core@shell structure is observed. With a higher amount of precursor, i.e., 2.0 mmol of $Fe(CO)_5$, corresponding to 38 min of injection time, the NP size increases up to 18.3 ± 1.1 nm. When the amount of Fe precursor is further increased to 2.4 mmol, corresponding to 45 min of injection time, larger NPs with diameter of

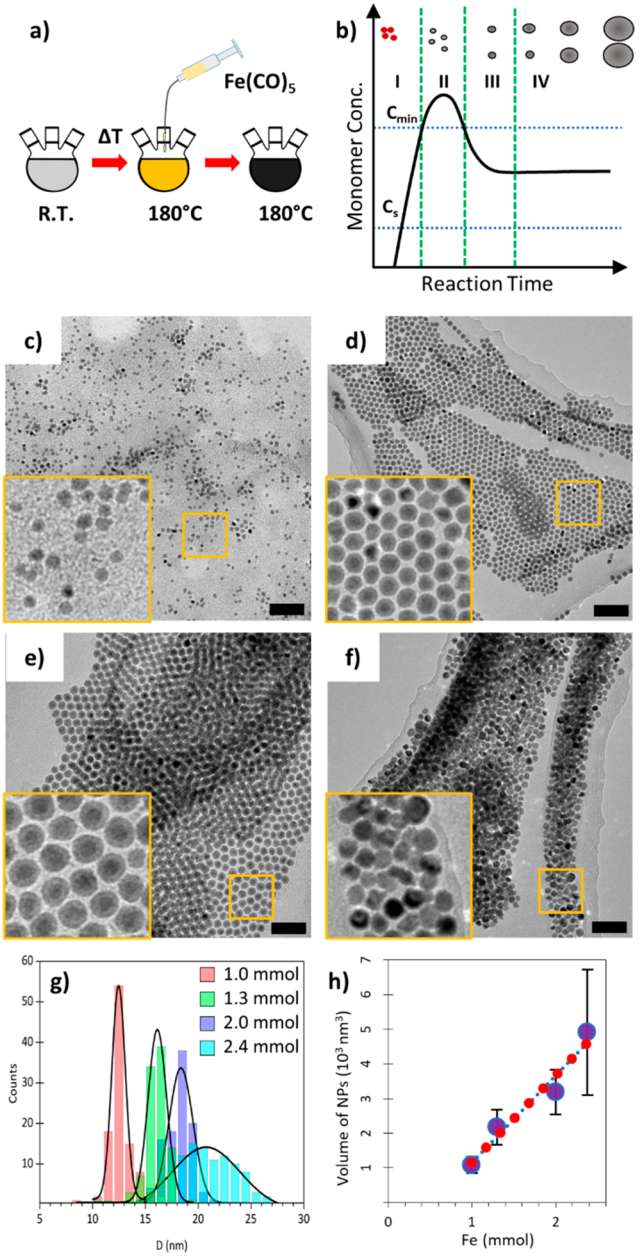

Figure 1. (a) Schematic illustration of the synthesis. (b) Extended LaMer plot configuration. TEM images of Fe NPs and relative zoom-in inset of the yellow square for 1.0 (c), 1.3 (d), 2.0 (e), and 2.4 mmol (f) of $Fe(CO)_5$ used. The scale bars in all four pictures correspond to 50 nm. (g) Size distribution for the four reactions with different amount of precursor used. (h) Relationship between NP volume and the amount of $Fe(CO)_5$ injected into the system.

20.7 ± 3.9 nm are obtained. The polydispersity values remained almost constant for the first three samples (standard deviation below 10%), while the standard deviation of the 20.7 nm NP size reaches a value close to 20% (Figure 1g). By plotting the volume of the NPs against the amount of $Fe(CO)_5$ injected in the reaction, the linear increase in size with the injection of the precursor shows that the size of α-Fe@Fe_xO_y NPs can be systematically tuned by controlling the amount of precursor used, as shown in Figure 1h. However, the NP growth tends to lose control due to a stronger interparticle magnetic dipole interaction when the NP size approaches 20 nm, causing them to aggregate. This ultimately leads to a

DOI: 10.1021/acs.chemmater.8b04056
Chem. Mater. 2018, 30, 8897−8904

broader size distribution, similar to previous reports with ferromagnetic metals.[22,23]

Among the parameters affecting the reaction, we found that important variables for the system are the rate of addition of the precursor and the amount of HDA-Cl present in solution, while a less important role is played by the amount of OAm. With regard to the rate of addition, we found that 0.4 mL/h is slow enough to lead a controlled synthesis without multiple nucleation events. With a faster rate of injection, the obtained NPs are polydisperse and multiple nucleation events occur (Figure S1). Slowing down the rate to 0.2 mL/h still produces highly monodispersed NPs but requires longer reaction times (Figure S2). In addition, the amount of Cl^- present in the solution drastically changes the reaction kinetics. The higher the concentration of Cl^- is, the larger the amount of Fe precursor needed to achieve similar sizes that are achieved with less Cl^-.

With 0.5 mmol of HDA-Cl the solution turns black in about 15 min, while when double the amount of HDA-Cl, it doubles the time for the solution to turn black. This can be explained by considering that in similar systems halogen ions interact with Fe monomers slowing down the nucleation and growth of the nanocrystals.[24]

Figure 2 shows the HAADF-STEM and EDS elemental mapping images of the NPs synthesized using 1.3 mmol of $Fe(CO)_5$ (25 min of injection time). The HAADF-STEM image confirms the NPs have a distinct core@shell structure with a darker shell surrounding a brighter core as shown in Figure 2a. Oxygen seems to be localized at the shell region, while Fe is rich in the core region (Figure 2b–d). The same structural feature can be observed in the NPs synthesized using different amounts of Fe precursor as shown in Figure S3.

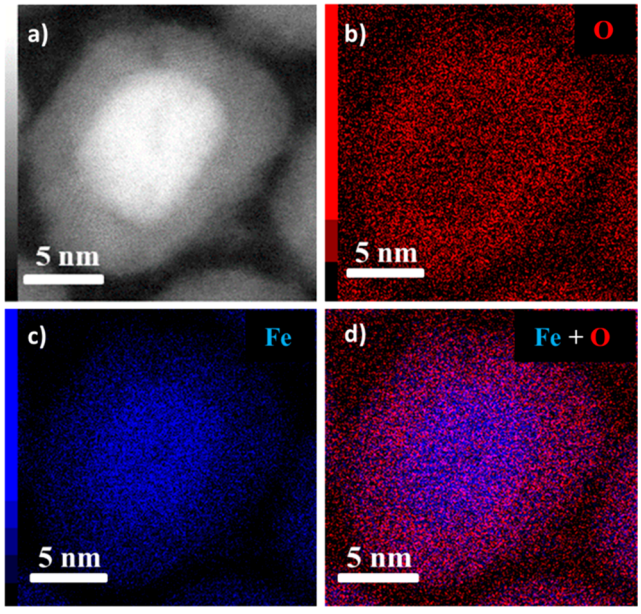

Figure 2. (a) HAADF-STEM images of one Fe NP synthesized using 1.3 mmol of $Fe(CO)_5$. EDS elemental mapping is also shown where signal intensities coming from (b) oxygen and (c) iron were detected. (d) An overlapping of the signals coming from the two elements.

Figure 3a shows the high-resolution HAADF-STEM image of a single NP. The lattice spacing of 2.0 Å was clearly observed in the core region, which corresponds to the (110) spacing of bcc Fe (α-Fe) phase. On the other hand, a lattice spacing of 2.5 Å was observed in the shell region corresponding to the (311) spacing of iron oxides such as Fe_3O_4 or γ-Fe_2O_3. In addition, the shell is found to be polycrystalline in nature. Full analysis of the HAADF-STEM image at the shell region revealed the existence of an ~4 nm crystalline domain viewed down the [100] zone axis of the inverse spinel crystal structure (Figure 3b,c). Analysis of the crystallite sizes in the oxide shell shows that the crystallite size is approximately of the same size as the shell thickness. The shell is made of small polycrystalline oxidized domains formed via the lattice expansion that occurs upon oxidation from α-Fe to the inverse spinel structure of Fe_3O_4/γ-Fe_2O_3. Figure 4 shows the XRD patterns of the four samples. The sample synthesized with the lowest amount of Fe precursor (shortest injection time) has no peak corresponding to α-Fe, while the peaks that originated from iron oxides are seen. The primary peak at 35° is attributed to the (311) plane of Fe_3O_4/γ-Fe_2O_3. Although it is difficult to assign the rest of the peaks present in the XRD pattern because the pattern is quite noisy, the absence of any peak corresponding to metallic Fe phases including α-Fe, γ-Fe, and δ-Fe confirms the complete oxidation of the NPs.

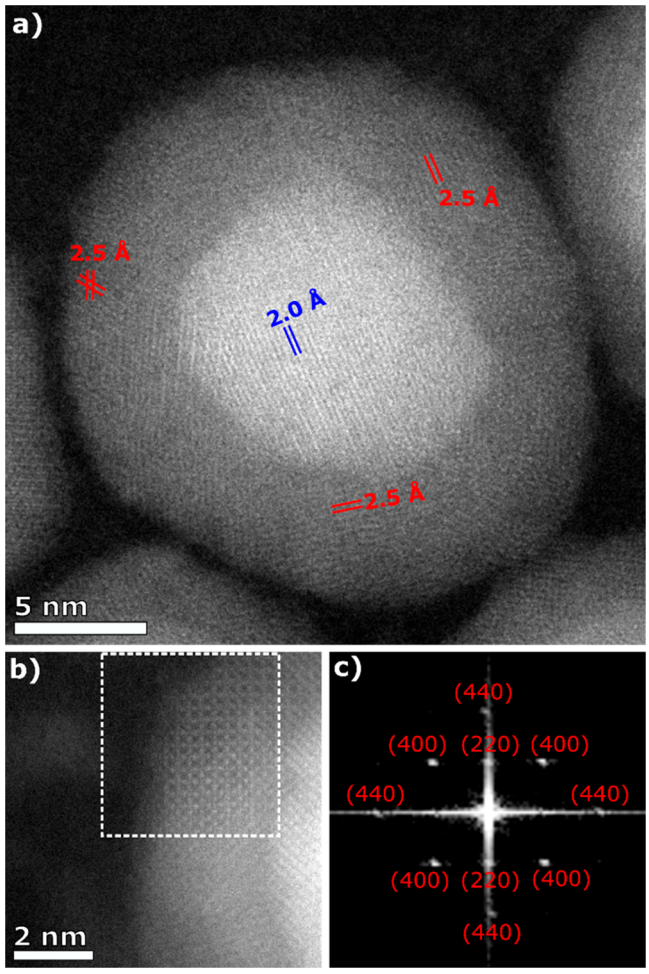

Figure 3. (a) High-resolution HAADF-STEM image of a core@shell NP, with the lattice spacing of Fe_3O_4/γ-Fe_2O_3 in red and α-Fe in blue. (b) An area of the oxide shell, with (c) the corresponding indexed FFT from the dashed white box.

In the cases of other samples, the peaks of the α-Fe phase become dominant and peaks related to oxides become

DOI: 10.1021/acs.chemmater.8b04056
Chem. Mater. 2018, 30, 8897–8904

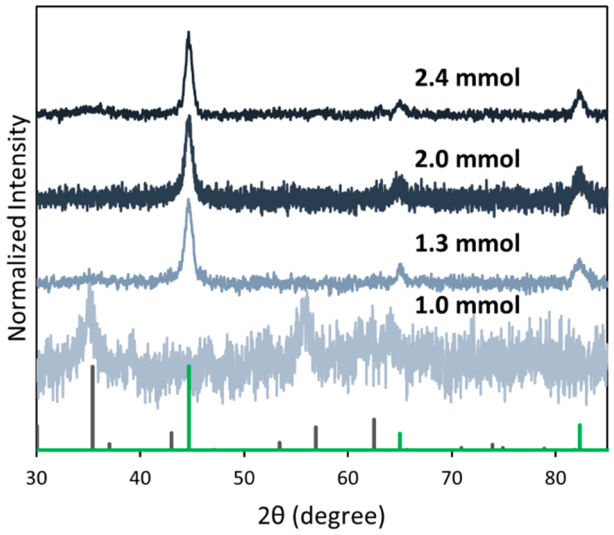

Figure 4. XRD patterns of the Fe NPs synthesized using different amounts of $Fe(CO)_5$. The dark gray reference pattern corresponds to Fe_3O_4 phase and the green one to bcc-Fe phase (JSPC PDF No. 01-079-0418 and 00-006-06969, respectively).

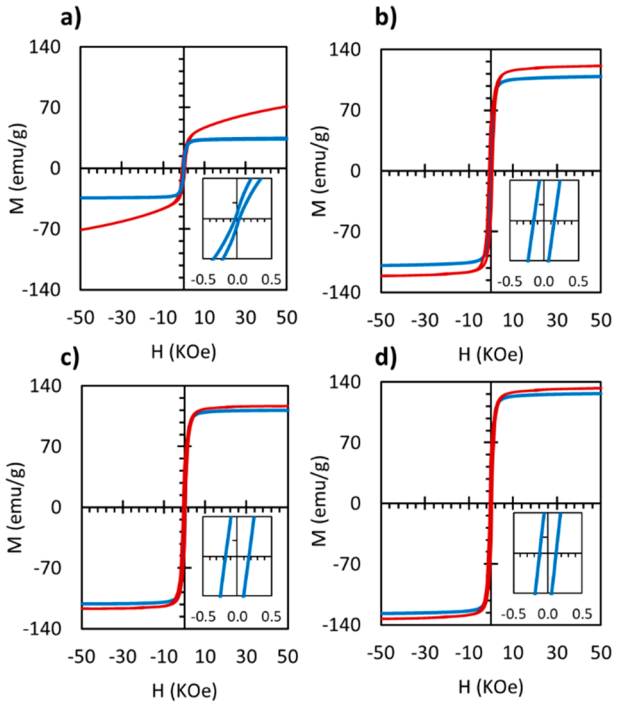

Figure 5. Magnetic hysteresis loop taken at 300 K (blue line) and 5 K (red line) with relative zoom-in at low fields for the four samples: (a) 1.0, (b) 1.3, (c) 2.0, and (d) 2.4 mmol of $Fe(CO)_5$ used.

negligibly weak. This is due to the small size of the Fe_xO_y grains, which translates into broader and less intense peaks in the XRD pattern compared to the peaks coming from α-Fe. XPS analyses revealed that the NPs synthesized with the lowest amount of Fe precursor (shortest injection time) exhibit no peak corresponding to Fe^0, while other samples clearly show the presence of Fe^0 supporting the above-mentioned discussion (Figure S4).

The mean crystalline sizes of α-Fe phase for NPs synthesized using 1.3, 2.0, and 2.4 mmol of $Fe(CO)_5$ (corresponding to 25, 38, and 45 min of injection time) were estimated using the (110) peak. The values for each sample are calculated to be 11.0, 11.4, and 13.2 nm, respectively. Those values are in good agreement with the average core sizes determined from the TEM analysis (see Table S1), suggesting that the Fe core is monocrystalline. From both XRD and TEM analysis, the mean size values of the Fe core follow an increasing trend along the four reactions, indicating that after the nucleation event the formed seeds act as primary sites for the growth of Fe NPs as single crystal while more Fe precursor is added.

Magnetic Properties. The magnetic properties of the four samples were analyzed via SQUID-VSM. Figure 5 shows the hysteresis loops at 300 K, and the main magnetic parameter are summarized in Table S1. An increasing trend for the value of M_s is related to the increase in size of the NPs. The smallest NPs (12.6 nm) show a value of 35 emu/g, which is the lowest of the series (Figure 5a). When the size of NPs increased from 12.6 to 15.9 nm, the M_s value jumped from 35 to 109 emu/g (Figure 5b), while a very high saturation magnetization for magnetite NPs reported has 88 emu/g.[25] For the NPs of mean size of 18.3 nm, the NPs gave a similar M_s value of 112 emu/g (Figure 5c). In the case of the largest NPs (20.7 nm), the M_s value reached 127 emu/g (Figure 5d). The behavior can be explained by considering that, in the first case, the NPs are completely oxidized, hence the lower M_s value. However, this value is much smaller than the value reported for NPs of similar size composed of monocrystalline magnetite phase.[26] This is due to the rapid oxidation process and the subsequent formation of multigrains of small iron oxide nanocrystals leading to the low M_s value. When the size increases, M_s value goes up due to the presence of highly crystalline α-Fe core. While the 15.9 and 18.3 nm NPs show similar M_s values, the largest NPs (20.7 nm) show the highest M_s value due to the presence of larger ferromagnetic cores.[27] The measured M_s values were used to estimate the volumes of α-Fe phase and oxide phases as described in the Supporting Information (eq S2). The iron oxide shell thickness remains almost constant along the whole series, while the Fe core diameter increases, similarly to the values reported in the TEM analysis (Table S1). The slight difference in obtained values between two different techniques can be explained by the spin canting effects present on the surface of the NPs which impairs the M_s in nanosized materials compared to the bulk counterparts,[28] leading to smaller estimated size.

The coercivity of 12.6 nm NPs of 30 Oe indicates extensive oxidation, while in the case of larger particles where the core@shell structure is maintained the coercivity increases to around 150 Oe; these values are in agreement with other reported works.[3,24,29]

Ligand Exchange and Hyperthermia Performance. To evaluate the performances of magnetic NPs in biomedical applications, it is necessary to transfer the NPs into water, and this process is performed via ligand exchange. Two kinds of NPs (15.9 and 18.3 nm NPs) were chosen which were respectively synthesized using 1.3 and 2.0 mmol of $Fe(CO)_5$. Those NPs have similar magnetic properties (M_s and coercivity), structural properties, oxide shell thickness, and similar polydispersity, differing in the size of Fe core. Other NPs (12.6 and 20.7 nm NPs, obtained using respectively 1.0 and 2.4 mmol of precursor) were not studied because the former was heavily oxidized (no Fe core), and the latter was polydisperse in size and colloidally unstable.

DOI: 10.1021/acs.chemmater.8b04056
Chem. Mater. 2018, 30, 8897−8904

To carry out this procedure, a dopamine-functionalized polymer[21] was chosen. PIMA is easy to functionalize through the nucleophilic substitution of its anhydride moieties with amines or other nucleophiles. Via this method, dopamine molecules can be easily inserted in the polymer chain to surface functionalize iron oxide and replace the native OAm through the catechol group.[25,30] In this study, the polymer used was adapted to this system. Indeed, compared to pure iron oxide NPs, Fe NPs possess higher M_s and soft ferromagnetic features making the system more prone to interparticle interactions, which could prove challenging for an effective ligand exchange process. To overcome this issue, the polymer synthesis was designed to have just one or two anchoring points (Figure S5) in each polymer chain to avoid any interlinking among NPs during the ligand exchange. In addition, the ligand exchange reaction was performed under low concentration conditions. Once the ligand exchange takes place, the remaining anhydride moieties are hydrolyzed with OH^-. This process makes the system water dispersible and converts each maleic anhydride unit in two carboxylic acid groups, allowing the stabilization of the NPs in water by steric and electrostatic repulsion. The resulting aqueous dispersion of NPs was analyzed by DLS as shown in Figure S7. The system was found to be stable over a broad range of pH (pH 4−10) and up to 150 mM of NaCl solution which makes the system suitable for use in biomedical applications (Figures S7 and S8).

Figures 6a and 6b show TEM images of 15.9 and 18.3 nm NPs taken after the ligand exchange, respectively. In the case of the 15.9 nm NPs (1.3 mmol of precursor), significantly shrunk cores and some hollow NPs are observed, in contrast to the core@shell structure shown in Figure 1d. For the 18.3 nm NPs, distinct core@shell structure is retained, and the formation of void can be observed.

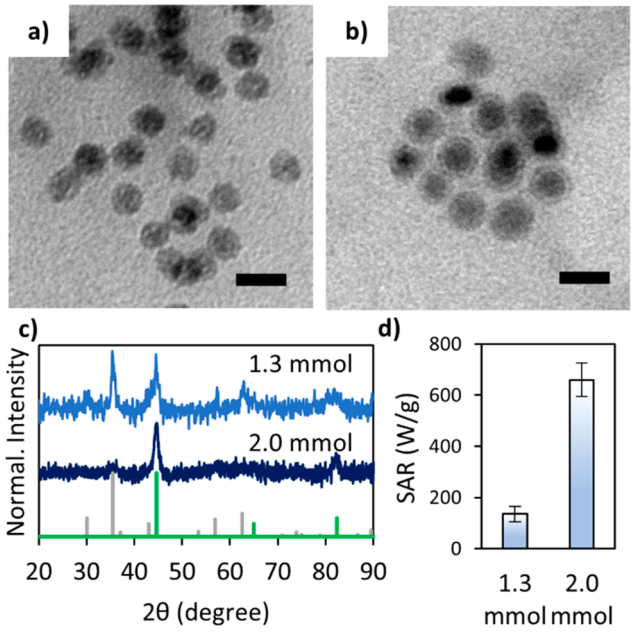

Figure 6. Characterization of the samples after ligand exchange: TEM picture of Fe NPs synthesized with (a) 1.3 and (b) 2.0 mmol of $Fe(CO)_5$; the scale bar corresponds to 20 nm. (c) XRD patterns shown with the gray reference pattern corresponding to the Fe_3O_4 phase and the green one to the Fe phase. (d) Heating power for the two systems measured at 303 kHz and 24 kA m^{-1}. Error bars indicate the standard error of the means of different SAR measurements.

To confirm this observation, the XRD patterns of 15.9 and 18.3 nm NPs after the ligand exchange were recorded. As shown in Figure 6c, the XRD pattern of 15.9 nm NPs shows two different phases present being metal (α-Fe) and oxide (Fe_3O_4/γ-Fe_2O_3), indicating that the NPs further oxidized during the ligand exchange reaction, while no iron oxide peak was detected on the XRD pattern before ligand exchange (Figure 4). The 18.3 nm NPs show no sign of significant oxidation with α-Fe still being the main phase present. However, the (110) peak of α-Fe becomes broader after the ligand exchange. The Fe core sizes estimated from TEM images and the XRD peak are both around 10 nm, which is smaller than the core size before ligand exchange, indicating that a certain extent of oxidation occurred.

Finally, the heating efficiency of the particles was evaluated by magnetic hyperthermia measurement. For the 15.9 nm NPs it was observed a SAR value of 135 W g^{-1}_{Fe}, while the 18.3 nm NPs showed a significant increase of SAR value at 660 W g^{-1}_{Fe}, ILP = 3.6 (Figure 6d and Table 2). The SAR value for the 15.9 nm NPs is similar to reported values for Fe NPs dispersed in water.[3,14] For the 18.3 nm NPs in water, on the other hand, the SAR output value was found to be 4 times higher than that of 15.9 nm NPs. This behavior can be explained by the different composition of the NPs. Indeed, the 18.3 nm NPs are big enough to retain α-Fe core even after ligand exchange. From theoretical study done by Habib et al. it was found that a diameter around 10 nm would maximize the hyperthermic effect of Fe NPs.[31] This size is very close to the size of Fe cores (10 nm) in our 18.3 nm NPs. Further, to investigate the stability of the system, we repeated the experiment after 2 months; no clear difference was detected in the ILP value (3.8), and no change in the structure was observed in the TEM (Figure S9).

Table 2. Magnetic Hyperthermia Measurements for 18.3 nm NPs (2.0 mmol) and Relative Conditions Used

measurement	freq (kHz)	field (kA m^{-2})	SAR (W g^{-1})	ILP (nHm^2 kg^{-1})
1	303	24.5	660	3.6
2 (after 2 months)	303	24.5	696	3.8
3	150	33.3	583	3.5
4	150	24.5	343	3.8
5	163	31.1	498	3.2

It is important for clinical application that the field and frequency used are within the safe limit.[32] Various fields and frequencies were chosen so that the product ($H \times f$) is lower than 5×10^9 A m^{-1}. The SAR and ILP values were obtained for 18.3 nm NPs as shown in Table 2. Our Fe NPs produce high heating efficiency with ILP of 3.2−3.8, which is one of the highest values reported so far for this type of material in similar conditions.[7,33]

Oxidation of Fe NPs. After the synthesis, Fe NPs are exposed to ambient environment, and they quickly oxidized to form an Fe_xO_y layer with a thickness of around 3−4 nm. This value showed no significant dependence on NPs size. Similar values have been reported for both crystalline[3] and amorphous[12] Fe NPs, and oxygen diffusion can be responsible for the formation of the first few monolayers of oxide.[34] However, the concentration of oxygen decreases with depth, and a further thickening process of the oxide layer is associated with the Kirkendall effect where the outward diffusion rate of

DOI: 10.1021/acs.chemmater.8b04056
Chem. Mater. 2018, 30, 8897−8904

Fe ions in the oxide layer becomes much larger than the inward diffusion rate of oxygen.[35] In an attempt to quantify this phenomenon, Sun et al. showed that the formation of the first oxide layers is rapid (below 1 ns), and in the presence of a Fe−Fe_xO_y interface the oxidation proceeds via formation of cationic vacancies in the a Fe crystal. Once enough vacancies are generated they start to coalesce, and ultimately, they form a void at the interface while the oxide layer thickens outward. The diffusion rate of Fe atoms is dependent on the temperature and the area of the Fe/Fe_xO_y interface so then when the voids start to form, the interfacial area starts to decrease and the rate of oxidation also decreases simultaneously.[36] In our study, no clear voids formation was observed for the as synthesized Fe NPs while after the ligand exchange step a reduction of Fe core was detected in both sample with brighter gaps between Fe and Fe_xO_y interface. Herman et al. showed that the removal of the native ligand on the surface of Fe@Fe_3O_4 facilitate the oxidation of the core/shell structures in air, favoring the Kirkendall effect.[4] The destabilization of the structure due to ligand displacement and possibly the change of the surrounding environment could explain the deeper oxidation in the case of water-dispersed NPs. However, the 18.3 nm Fe NPs can undergo the aforementioned process and still retain a Fe core because of the initial larger volume of α-Fe crystal compared to the smaller sample (15.9 nm). Combined with the high crystallinity of α-Fe, the larger residual core leads to significantly higher magnetic hyperthermia outcomes.

CONCLUSIONS

In this study, Fe@Fe_xO_y NPs with different sizes were synthesized, and their suitability for magnetic hyperthermia therapy was evaluated. Using a continuous injection of the precursor, this synthetic strategy can produce different sizes of NPs by tuning the amount of precursor injected. The nanocrystals formed are single crystal with a good size distribution, and once open to air, the formation of an iron oxide shell occurs. When the NPs are as small as 12 nm, mainly iron oxide NPs obtained, whereas with larger size a polycrystalline iron oxide shell is formed, retaining a single crystalline iron core. An upper limit for the size is reached around 20 nm, after which the system starts losing colloidal stability during the reaction, and subsequently the size distribution broadens. Two sets of NPs (15.9 and 18.3 nm) were functionalized with a dopamine-functionalized polymer, resulting in an efficient transfer of the NPs in to water. Moreover, the NPs dispersed in water were colloidally stable in a wide range of pH and ionic strength that can be found in physiological conditions. The 18 nm NPs possess excellent heating capabilities, being also stable in solution for 2 months with no sign of chemical deterioration. These results indicate a new avenue for producing stable and high heating efficiency nanoparticles that is much needed for hyperthermia and many other biomedical applications.

ASSOCIATED CONTENT

Supporting Information

The Supporting Information is available free of charge on the ACS Publications website at DOI: 10.1021/acs.chemmater.8b04056.

Additional data on all reactions; TEM micrographs; STEM-EDS elemental mapping micrographs; XPS spectra; H NMR spectrum; study of colloidal stability; summary table of nanoparticles properties; Scherrer equation; calculation of size of magnetic phase (PDF)

AUTHOR INFORMATION

Corresponding Authors

*E-mail: ntk.thanh@ucl.ac.uk.
*E-mail: shinya@jaist.ac.jp.

ORCID

Maximilian O. Besenhard: 0000-0002-5079-617X
Shinya Maenosono: 0000-0003-2669-8219
Nguyen Thi Kim Thanh: 0000-0002-4131-5952

Notes

The authors declare no competing financial interest.

ACKNOWLEDGMENTS

S.F. thanks UCL-JAIST for funding his PhD studentship, N.T.K.T. thanks AOARD (Grant FA2382-17-1-4042) and EPSRC for funding, and M.O.B. thanks the EPSRC (Grant EP/M015157/1).

REFERENCES

(1) López-Ortega, A.; Estrader, M.; Salazar-Alvarez, G.; Roca, A. G.; Nogués, J. Applications of Exchange Coupled Bi-Magnetic Hard/Soft and Soft/Hard Magnetic Core/Shell Nanoparticles. *Phys. Rep.* **2015**, *553*, 1−32.

(2) Khurshid, H.; Chandra, S.; Li, W.; Phan, M. H.; Hadjipanayis, G. C.; Mukherjee, P.; Srikanth, H. Synthesis and Magnetic Properties of Core/Shell FeO/Fe $_3$ O $_4$ Nano-Octopods. *J. Appl. Phys.* **2013**, *113* (17), 17B508.

(3) Lacroix, L.-M.; Frey Huls, N.; Ho, D.; Sun, X.; Cheng, K.; Sun, S. Stable Single-Crystalline Body Centered Cubic Fe Nanoparticles. *Nano Lett.* **2011**, *11* (4), 1641−1645.

(4) Herman, D. A. J.; Ferguson, P.; Cheong, S.; Hermans, I. F.; Ruck, B. J.; Allan, K. M.; Prabakar, S.; Spencer, J. L.; Lendrum, C. D.; Tilley, R. D. Hot-Injection Synthesis of Iron/Iron Oxide Core/Shell Nanoparticles for T 2 Contrast Enhancement in Magnetic Resonance Imagingw. *Chem. Commun.* **2011**, *47* (47), 9221−9223.

(5) Huber, D. L.; Venturini, E. L.; Martin, J. E.; Provencio, P. P.; Patel, R. J. Synthesis of Highly Magnetic Iron Nanoparticles Suitable for Field Structuring Using a β-Diketone Surfactant. *J. Magn. Magn. Mater.* **2004**, *278* (3), 311−316.

(6) Zhou, Z.; Sun, Y.; Shen, J.; Wei, J.; Yu, C.; Kong, B.; Liu, W.; Yang, H.; Yang, S.; Wang, W. Iron/Iron Oxide Core/Shell Nanoparticles for Magnetic Targeting MRI and near-Infrared Photothermal Therapy. *Biomaterials* **2014**, *35* (26), 7470−7478.

(7) Mehdaoui, B.; Meffre, A.; Lacroix, L. M.; Carrey, J.; Lachaize, S.; Gougeon, M.; Respaud, M.; Chaudret, B. Large Specific Absorption Rates in the Magnetic Hyperthermia Properties of Metallic Iron Nanocubes. *J. Magn. Magn. Mater.* **2010**, *322* (19), L49−L52.

(8) Takahashi, M.; Mohan, P.; Nakade, A.; Higashimine, K.; Mott, D.; Hamada, T.; Matsumura, K.; Taguchi, T.; Maenosono, S. Ag/FeCo/Ag Core/Shell/Shell Magnetic Nanoparticles with Plasmonic Imaging Capability. *Langmuir* **2015**, *31* (7), 2228−2236.

(9) Matsumura, K.; Takakura, M.; Arai, H.; Taguchi, T.; et al. Magnetic Separation of Autophagosomes from Mammalian Cells Using Magnetic − Plasmonic Hybrid Nanobeads. *ACS Omega* **2017**, *2* (8), 4929−4937.

(10) Mehdaoui, B.; Meffre, A.; Carrey, J.; Lachaize, S.; Lacroix, L. M.; Gougeon, M.; Chaudret, B.; Respaud, M. Optimal Size of Nanoparticles for Magnetic Hyperthermia: A Combined Theoretical and Experimental Study. *Adv. Funct. Mater.* **2011**, *21* (23), 4573−4581.

(11) Huber, D. L. Synthesis Properties, and Applications of Iron Nanoparticles. *Small* **2005**, *1* (5), 482−501.

DOI: 10.1021/acs.chemmater.8b04056
Chem. Mater. 2018, 30, 8897−8904

(12) Peng, S.; Wang, C.; Xie, J.; Sun, S. Synthesis and Stabilization of Monodisperse Fe Nanoparticles. *J. Am. Chem. Soc.* **2006**, *128* (33), 10676−10677.
(13) Cheong, S.; Ferguson, P.; Hermans, I. F.; Jameson, G. N. L.; Prabakar, S.; Herman, D. A. J.; Tilley, R. D. Synthesis and Stability of Highly Crystalline and Stable Iron/Iron Oxide Core/Shell Nanoparticles for Biomedical Applications. *ChemPlusChem.* **2012**, *77* (2), 135−140.
(14) Nemati, Z.; Alonso, J.; Khurshid, H.; Phan, M. H.; Srikanth, H. Core/Shell Iron/Iron Oxide Nanoparticles: Are They Promising for Magnetic Hyperthermia? *RSC Adv.* **2016**, *6* (45), 38697−38702.
(15) Vreeland, E. C.; Watt, J.; Schober, G. B.; Hance, B. G.; Austin, M. J.; Price, A. D.; Fellows, B. D.; Monson, T. C.; Hudak, N. S.; Maldonado-Camargo, L.; et al. Enhanced Nanoparticle Size Control by Extending LaMer's Mechanism. *Chem. Mater.* **2015**, *27* (17), 6059−6066.
(16) Peng, X.; Wickham, J.; Alivisatos, A. P. Kinetics of II-VI and III-V Colloidal Semiconductor Nanocrystal Growth: "Focusing" of Size Distributions [15]. *J. Am. Chem. Soc.* **1998**, *120*, 5343−5344.
(17) Takahashi, M.; Higashimine, K.; Mohan, P.; Mott, D. M.; Maenosono, S. Formation Mechanism of Magnetic−plasmonic Ag@FeCo@Ag Core−shell−shell Nanoparticles: Fact Is More Interesting than Fiction. *CrystEngComm* **2015**, *17*, 6923−6929.
(18) Lamer, V. K.; Dinegar, R. H. Theory, Production and Mechanism of Formation of Monodispersed Hydrosols. *J. Am. Chem. Soc.* **1950**, *72* (11), 4847−4854.
(19) Zhang, S.; Jiang, G.; Filsinger, G. T.; Wu, L.; Zhu, H.; Lee, J.; Wu, Z.; Sun, S. Halide Ion-Mediated Growth of Single Crystalline Fe Nanoparticles. *Nanoscale* **2014**, *6* (9), 4852−4856.
(20) Kallumadil, M.; Tada, M.; Nakagawa, T.; Abe, M.; Southern, P.; Pankhurst, Q. A. Suitability of Commercial Colloids for Magnetic Hyperthermia. *J. Magn. Magn. Mater.* **2009**, *321* (10), 1509−1513.
(21) Wang, W.; Ji, X.; Na, H. B.; Safi, M.; Smith, A.; Palui, G.; Perez, J. M.; Mattoussi, H. Design of a Multi-Dopamine-Modified Polymer Ligand Optimally Suited for Interfacing Magnetic Nanoparticles with Biological Systems. *Langmuir* **2014**, *30* (21), 6197−6208.
(22) Lagrow, A. P.; Ingham, B.; Toney, M. F.; Tilley, R. D. Effect of Surfactant Concentration and Aggregation on the Growth Kinetics of Nickel Nanoparticles. *J. Phys. Chem. C* **2013**, *117* (32), 16709−16718.
(23) Bleier, G. C.; Watt, J.; Simocko, C. K.; Lavin, J. M.; Huber, D. L. Reversible Magnetic Agglomeration: A Mechanism for Thermodynamic Control over Nanoparticle Size. *Angew. Chem., Int. Ed.* **2018**, *57* (26), 7678−7681.
(24) Yang, Z.; Zhao, T.; Huang, X.; Chu, X.; Tang, T.; Ju, Y.; Wang, Q.; Hou, Y.; Gao, S. Modulating the Phases of Iron Carbide Nanoparticles: From a Perspective of Interfering with the Carbon Penetration of Fe@Fe $_3$ O $_4$ by Selectively Adsorbed Halide Ions. *Chem. Sci.* **2017**, *8* (1), 473−481.
(25) Hachani, R.; Lowdell, M.; Birchall, M.; Hervault, A.; Mertz, D.; Begin-Colin, S.; Thanh, N. T. K. Polyol Synthesis, Functionalisation, and Biocompatibility Studies of Superparamagnetic Iron Oxide Nanoparticles as Potential MRI Contrast Agents. *Nanoscale* **2016**, *8* (6), 3278−3287.
(26) Santoyo Salazar, J.; Perez, L.; De Abril, O.; Phuoc, L. T.; Ihiawakrim, D.; Vazquez, M.; Greneche, J.-M.; Begin-Colin, S.; Pourroy, G. Magnetic Iron Oxide Nanoparticles in 10−40 Nm Range: Composition in Terms of Magnetite/Maghemite Ratio and Effect on the Magnetic Properties. *Chem. Mater.* **2011**, *23*, 1379−1386.
(27) Majetich, S. A.; Wen, T.; Mefford, O. T. Magnetic Nanoparticles. *MRS Bull.* **2013**, *38* (11), 899−903.
(28) Morales, M. P.; Veintemillas-Verdaguer, S.; Montero, M. I.; Serna, C. J.; Roig, A.; Casas, L.; Martínez, B.; Sandiumenge, F. Surface and Internal Spin Canting in γ-Fe 2 O 3 Nanoparticles. *Chem. Mater.* **1999**, *11* (11), 3058−3064.
(29) McGrath, A. J.; Cheong, S.; Henning, A. M.; Gooding, J. J.; Tilley, R. D. Size and Shape Evolution of Highly Magnetic Iron Nanoparticles from Successive Growth Reactions. *Chem. Commun.* **2017**, *53* (84), 11548−11551.
(30) Xu, C.; Xu, K.; Gu, H.; Zheng, R.; Liu, H.; Zhang, X.; Guo, Z.; Xu, B. Dopamine as a Robust Anchor to Immobilize Functional Molecules on the Iron Oxide Shell of Magnetic Nanoparticles. *J. Am. Chem. Soc.* **2004**, *126* (32), 9938−9939.
(31) Habib, A. H.; Ondeck, C. L.; Chaudhary, P.; Bockstaller, M. R.; McHenry, M. E. Evaluation of Iron-Cobalt/Ferrite Core-Shell Nanoparticles for Cancer Thermotherapy. *J. Appl. Phys.* **2008**, *103* (7), 305−308.
(32) Muela, A.; Muñoz, D.; Martín-Rodríguez, R.; Orue, I.; Garaio, E.; Abad Díaz de Cerio, A.; Alonso, J.; García, J. A.; Fdez-Gubieda, M. L. Optimal Parameters for Hyperthermia Treatment Using Biomineralized Magnetite Nanoparticles: Theoretical and Experimental Approach. *J. Phys. Chem. C* **2016**, *120* (42), 24437−24448.
(33) Blanco-Andujar, C.; Walter, A.; Cotin, G.; Bordeianu, C.; Mertz, D.; Felder-Flesch, D.; Begin-Colin, S. Design of Iron Oxide-Based Nanoparticles for MRI and Magnetic Hyperthermia. *Nanomedicine* **2016**, *11* (14), 1889−1910.
(34) Yang, D.-Q.; Gillet, J.-N.; Meunier, M.; Sacher, E. Room Temperature Oxidation Kinetics of Si Nanoparticles in Air, Determined by x-Ray Photoelectron Spectroscopy. *J. Appl. Phys.* **2005**, *97* (2), No. 024303.
(35) Wang, C. M.; Baer, D. R.; Thomas, L. E.; Amonette, J. E.; Antony, J.; Qiang, Y.; Duscher, G. Void Formation during Early Stages of Passivation: Initial Oxidation of Iron Nanoparticles at Room Temperature. *J. Appl. Phys.* **2005**, *98* (9), No. 094308.
(36) Sun, Y.; Zuo, X.; Sankaranarayanan, S. K. R. S.; Peng, S.; Narayanan, B.; Kamath, G. Quantitative 3D Evolution of Colloidal Nanoparticle Oxidation in Solution. *Science* **2017**, *356* (6335), 303−307.

DOI: 10.1021/acs.chemmater.8b04056
Chem. Mater. 2018, 30, 8897−8904